Mn²⁺-Doped Prussian Blue Nanocubes for Bimodal Imaging and Photothermal Therapy with Enhanced Performance

Wenwen Zhu,[†,‡] Kai Liu,[†,‡] Xiaoqi Sun,[‡] Xin Wang,[§] Yonggang Li,[§] Liang Cheng,*[,‡] and Zhuang Liu[‡]

[‡]Institute of Functional Nano & Soft Materials Laboratory (FUNSOM), Jiangsu Key Laboratory for Carbon-Based Functional Materials & Devices, Collaborative Innovation Center of Suzhou Nano Science and Technology, Soochow University, Suzhou, Jiangsu 215123, China

[§]Department of Radiology the First Affiliated Hospital of Soochow University Suzhou, Jiangsu 215006, China

S Supporting Information

ABSTRACT: Prussian blue (PB) as a clinically adapted agent recently has drawn much attention in cancer theranostics for potential applications in magnetic resonance (MR) imaging as well as photothermal cancer treatment. In this work, we take a closer look at the imaging and therapy performance of PB agents once they are doped with Mn^{2+}. It is found that Mn^{2+}-doped PB nanocubes exhibit increased longitudinal relaxivity along with enhanced optical absorption red-shifted to the near-infrared (NIR) region. Those properties make PB:Mn nanocubes with appropriate surface coatings rather attractive agents for biomedical imaging and cancer therapy, which have been successfully demonstrated in our in vivo experiments for effectively tumor ablation.

KEYWORDS: Prussian blue, Mn doping, MR imaging, photoacoustic imaging, photothermal therapy
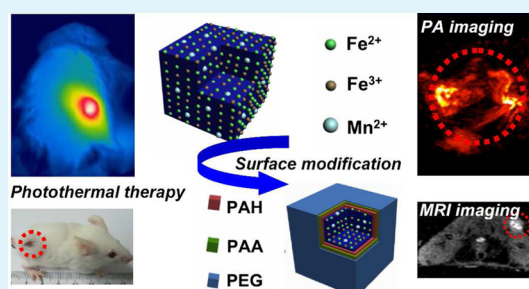
INTRODUCTION

Prussian blue (PB) is a U.S. Food and Drug Administration (FDA) approved agent for clinical use in the treatment of radioactive exposure.[1,2] In recent years, PB-based nanoagents have been reported as photothermal therapy (PTT) agents because their high optical absorbance peaked at ~700 nm.[3,4] Compared with other inorganic PTT agents including carbon-based nanomaterials,[5−9] noble metal-based nanostructures,[10−15] as well as transition-metal sulfides and oxides,[16−19] which in general are not biodegradable and thus have tremendous difficulties in terms of clinical translation, PB is already a clinically approved agent and can be obtained with low costs. Therefore, many groups including ours have explored the applications of PB-based nanoagents as PTT agent for cancer treatment in animal models.[20−28] Further, it has been found that doping of other paramagnetic ions, such as Gd^{3+} and Mn^{2+} into PB could enhance its T1 contrasting ability in magnetic resonance (MR) imaging.[29−34] However, the applications of such Gd- or Mn-doped PB nanostructures in terms of improving therapy and imaging performance at the same time have not yet been demonstrated in vivo to the best of our knowledge.

This work as a revisit of Mn-doped PB (PB:Mn) nanostructures would like to carefully look into how the optical and magnetic properties of PB are tuned by Mn^{2+} doping, and explore in vivo applications of such nanoagent after appropriate surface engineering for bimodal imaging and photothermal cancer treatment (Figure 1a). It was found that Mn^{2+}-doped PB nanocubes fabricated in this work, on one hand possess an improved photothermal effect resulting from their increased optical absorption red-shifted to the near-infrared (NIR) region, on the other hand exhibit higher longitudinal relaxivity (r1), which is preferred for T1-weighted MR imaging. After coating with polyethylene glycol (PEG) via a layer-by-layer (LBL) polymer coating and conjugation strategy, PEGylated PB:Mn nanocubes were obtained and used for in vivo bimodal MR & photoacoustic (PA) imaging and photothermal cancer treatment, achieving a great tumor ablation therapeutic effect in a mouse tumor modal. Our results highlight the great promise of Mn^{2+}-doped PB nanostructures for applications as a safe and effective nanoscale theranostic agent, which may have a substantial potential for future clinical translation.

EXPERIMENTAL SECTION

Materials. $FeCl_3·6H_2O$, $MnCl_2·4H_2O$, $K_4[Fe(CN)_6]·3H_2O$, and citric acid were obtained from Sinopharm Chemical Reagent CO., Ltd. (China) and used as received. Polyacrylic acid (PAA, $M_w ≈ 1800$), poly(allylamine hydrochloride) (PAH, $M_w ≈ 15\,000$), 1-(3-(dimethylamino)propyl)-3-ethylcarbodiimide hydrochloride (EDC), propidium iodide (PI), 3-(4,5-dimethylthiazol-2-yl)-2,5-diphenyltetrazolium bromide (MTT), and calcein acetoxymethyl ester (Calcein AM) were obtained from Sigma-Aldrich. Amino group terminated glycol (PEG-NH₂, $M_w ≈ 5000$) was obtained from (Biomatrik Inc.). Aqueous solutions were prepared with deionized water (18.2 MΩ cm) collected from a Milli-Q system.
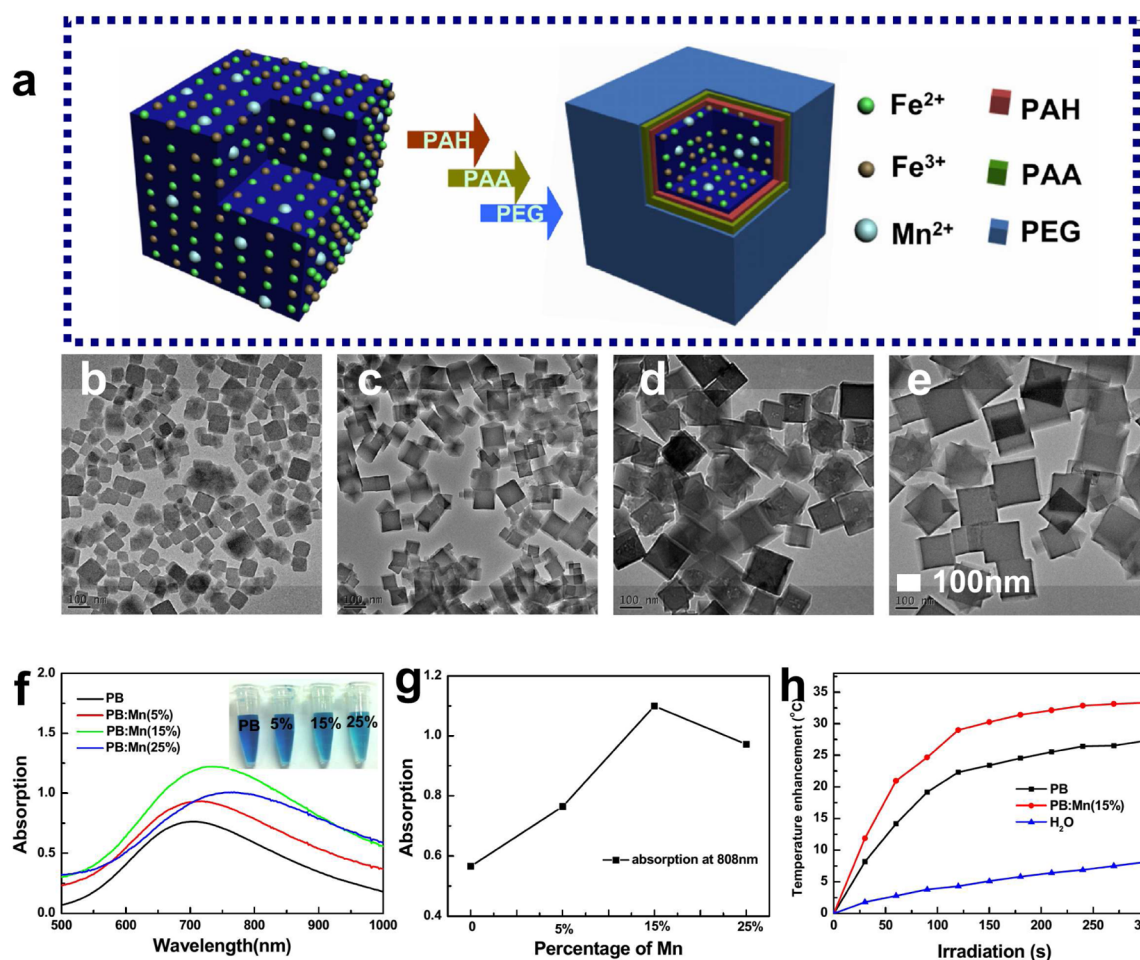
Figure 1. PB:Mn nanocubes synthesis and characterization. (a) Scheme illustration for the synthesis of PB:Mn-PEG. (b−e) TEM images of PB:Mn-PEG nanocubes: (b) PB:Mn(0%), (c) PB:Mn(5%), (d) PB:Mn(15%), (e) PB:Mn(25%). The scale bar is 100 nm. (f) UV−vis spectra of PB:Mn nanocubes with different ratios of Mn-doping. Inset: photos of PB:Mn solutions. (g) Absorption at 808 nm of PB:Mn nanocubes with different doping ratios of Mn solutions with the same concentration of metal ions (a sum of [Fe]+[Mn]). (h) Photothermal heating of PB and PB:Mn(15%) solutions at the same concentration of 0.05 mg/mL. The irradiation time was 5 min.

Synthesis of Mn-Doped PB Nanocubes. PB nanocubes were produced according to a previous protocol, whereas Mn^{2+}-doped PB nanocubes were synthesized with modifications.[35] In brief, to prepare PB nanocubes without Mn^{2+} doping, 0.5 mmol of citric acid was first added into 20 mL of water solution of $FeCl_3 \cdot 6H_2O$ (10 mM) at 60 °C, whereas 0.5 mmol citric acid was added into 20 mL of solution of $K_4[Fe(CN)_6] \cdot 3H_2O$ (1.0 mM) at 60 °C. The solution of $K_4[Fe(CN)_6] \cdot 3H_2O$ (1.0 mM) was dropwisely added into the solution of $FeCl_3 \cdot 6H_2O$ at 60 °C under magnetic stirring. The solution turned into bright blue gradually. After 5 min, the solution was cooled down to room temperature. To precipitate PB nanocubes from the solution, we added 10 mL of NaCl (0.5 M). Afterward, the solution was centrifuged at 14800 rpm for 10 min to collect PB nanocubes, which were then dispersed in water to form a solution at the concentration of 2.0 mg/mL. When producing Mn-doped PB nanocubes, all steps were the same except that a mixed solution of $FeCl_3 \cdot 6H_2O$ and $MnCl_2 \cdot 4H_2O$ at the desired ratio (see the Supporting Information, Table S1) was used to replace the $FeCl_3 \cdot 6H_2O$ solution used to synthesize PB nanocubes.

Surface Modification of PB:Mn Nanocubes. To increase the biocompatibility and physiological stability of PB:Mn nanocubes, we carried out surface modifications by the LBL polymer coating.[2,4] PB:Mn nanocubes were first modified with PAH and PAA in a layer-by-layer (LBL) manner via the electrostatic interaction and then were conjugated with PEG in the presence of EDC. In brief, 2 mmol of as-prepared negatively charged PB:Mn nanocubes were added into 8 mL solution of cationic polymer PAH ($M_w \approx 15\,000$, 4 mg/mL) under

magnetic stirring. Four h later, excess PAH polymer was removed by centrifugation at 14800 rpm for 5 min and washed with DI water for 2 times. The PAH coated PB:Mn nanocubes redispersed in water were then added with 4 mL solution of anionic polymer PAA ($M_w \approx 1800$, 4 mg/mL). Excess PAA was removed by centrifugation at 14800 rpm after 4 h with magnetic stirring. Thirty milligrams PEG-NH$_2$ ($M_w \approx 5000$) and 15 mg EDC were added into the solution of PB:Mn coated with PAH/PAA at pH ~7.4. After ultrasonication for 15 min, the reaction was kept under stirring overnight. PEGylated PB:Mn (PB:Mn-PEG) were then purified by centrifugation and redispersed in water for future use.

Characterization. Transmission electron microscopy (TEM, FEI Tecnai F20, acceleration voltage = 200 kV) was applied to characterize the shape and size of PB and PB:Mn nanocubes. Energy-dispersive X-ray spectroscopy (EDX) was carried out to acquire elemental information on our samples. X-ray diffraction (PANalytical X-ray diffractometer) equipped with Cuka radiation $\lambda = 0.15406$ nm) was used to acquire the information on crystallography and phase of as-prepared PB:Mn nanocubes. Fourier transform Infrared (FT-IR) spectra were obtained by HYPERION (German, Bruker) from 4000 to 400 cm^{-1}. UV−vis spectra were measured with a PerkiinElmer Lambda 750 UV−vis-NIR spectrophotometer. The sizes and zeta potentials of PB or PB:Mn nanocubes were measured with a Malvern zetasizer (ZEN3690, Malvern, UK). Concentrations of Fe and Mn were measured by inductively coupled plasma atomic emission spectroscopy (ICP-AES).

In Vitro Cytotoxicity Assay. 4T1 murine breast cancer cells were cultured in RPMI-1640 medium containing 10% fetal bovine serum (FBS) and 1% penicillin/streptomycin at 37 °C under 5% CO_2.

For in vitro cell toxicity assay, 4T1 cells were seeded in 96-well plates at a density of 1×10^4 cells per well and cultured at 37 °C overnight. Then, the cells were added with PB:Mn-PEG solutions with different concentrations and then incubated for 24 h. Then MTT solution (25 µL, 5 mg/mL) was added to each well and further incubated at 37 °C for another 4 h. After that, 150 µL of dimethyl sulfoxide (DMSO) was added into each well after carefully removing the original culture medium. After being shaken at room temperature for 10 min, the absorbance at 570 nm of each well was recorded by a microplate reader (model 680 Bio-RAD) to determine their relative cell viability.

Cell Internalization of PB:Mn(15%)-PEG. Internalization of PB:Mn(15%)-PEG by cells was measured with ICP-AES. 105 4T1 cells were seeded in the 35 mm culture dish and incubated at 37 oC overnight. One ml PB:Mn(15%)-PEG (0.2 mg/mL) was added. After incubating for various periods of time, cells were collected and washed with PBS for two times before being boiled in aqua regia supplemented of 25% perchloric acid. Afterward, the concentration of Fe in each sample, which was diluted into 10 mL by water, was measured by ICP-AES.

In Vitro PTT Efficacy of PB:Mn Nanocubes. The photothermal treatment effect of PB:Mn(15%)-PEG nanocubes was determined by using a standard MTT assay and live/dead dual staining assay. For MTT assay, 4T1 cells were seeded in 96-well plates at a density of 1×10^4 cells per well and cultured at 37 °C overnight. Then, the cells were incubated with fresh complete medium containing PB:Mn(15%)-PEG of 0.025, 0.05, 0.1, and 0.2 mg/mL, respectively, for 4 h before being irradiated by an 808 nm laser at 0.5 W/cm^2 or 0.8 W/cm^2 for 5 min. Afterward, the cells were incubated with MTT solution for additional 4 h before measuring its absorbance using the microplate reader as aforementioned.

For live/dead dual staining, 8×10^5 4T1 cells were seeded in the 35 mm culture dish and incubated at 37 °C for 24 h. Then, the cells was incubated with of PB:Mn(15%)-PEG at 0.025, 0.05, 0.1, and 0.2 mg/mL for 4 h, respectively, followed by being irradiated with the 808 nm laser for 5 min at 0.8 W/cm^{-2}. Fifteen min later, the cells were incubated with fresh medium containing Calcein-AM and PI at 1 and 3 µg/mL at 37 °C for 30 min before being imaged using a confocal laser scanning microscope (Leica SPII, Germany).

Tumor Modal. Balb/c mice were obtained from Nanjing Peng Sheng Biological Technology Co. Ltd. and used under protocols approved by Soochow University Laboratory Animal Center. The 4T1 tumors were generated by subcutaneous injection of 1×10^6 cells in ~30 µL serum-free RMPI-1640 medium onto the back of each female Balb/c mice. When the tumor size reached about 60 mm^3, in vivo experiments were then carried out.

In Vivo PA/MR Biomodal Imaging. 4T1 tumor-bearing mice were intravenously (i.v.) injected with PB: Mn(15%)-PEG at a dose of 20 mg/kg (body weight). PA and MR imaging were performed respectively at time points of 0 h, 1 h, and 24 h, respectively. PA images (Endra Nexus 128, Ann Arbor, MI) were taken while the mice were kept in a water system at 37.5 °C. MR images (GE Healthcare, USA) were taken under a 3.0 T magnetic field with a special coil for small animal imaging.

In Vivo Photothermal Therapy. Eight 4T1 tumor-bearing mice were involved in the *in vivo* experiment. Four mice were i.v. injected with PB:Mn(15%)-PEG at a dose of 20 mg/kg, while the other four were taken as the control group. After 24 h, the tumors were irradiated with an 808 nm laser at the power density of 0.8 W/cm^2 for 5 min. An infrared (IR) thermal camera was used to monitor the temperature at tumor site during the photothermal process. Eighteen days after injection of PB:Mn(15%)-PEG, the mice were sacrificed for toxicity evaluation. Major organs include liver, spleen, kidney, heart, and lung, were harvested, fixed in 10% neutral buffered formalin, processed into paraffin, and sectioned into 8 µm slices, which were then stained with H&E and imaged under a digital microscope (Leica Qwin).

■ RESULTS AND DISCUSSION

Mn^{2+}-doped PB with various doping ratios were synthesized by partly replacing $FeCl_3$ with $MnCl_2$ in a conventional procedure to produce PB nanocubes.[1,35] TEM images of the synthesized PB:Mn nanostructures are shown in Figure 1b−e. It could be found that the morphology of PB:Mn nanocubes with different Mn^{2+} doping ratios was all in cubic shape. The crystallography and phase information were acquired through X-ray diffraction (XRD) measurement from which PB:Mn nanocubes could be ascribed to be cubic (JCPDS. 52−1907) (see the Supporting Information, Figure S1), agreeing well with literature.[1] Also, from the XRD result of PB:Mn (50%), which was produced by mixing $K_4[Fe(CN)_6]$ with only $MnCl_2$ (no $FeCl_3$), it could be seen that replacing Fe^{3+} totally by Mn^{2+} did not change the crystal phase of PB, indicating that Fe^{3+} within the lattice structure of PB was likely replaced by Mn^{2+} in our Mn-doped PB samples, consistent to a number of previous reports.[29,30] Meanwhile, The sizes of PB:Mn nanocubes obtained with different doping rates of Mn^{2+} (0, 5, 15, and 25%, representing the feeding molar ratios of $[Mn]/([Mn] + [Fe])$ increased from 60 to 160 nm with the increased Mn^{2+} doping ratios (see the Supporting Information, Figure S2). The changes in size evidently revealed that more Mn^{2+} doping into the nanocubes could result in a larger size, which might result from the doping of Mn^{2+} ions with a larger ionic radius into the nanocube lattice.[33,34]

To confirm the successful Mn^{2+} doping, we show through energy-dispersive X-ray (EDX) analysis of the obtained PB:Mn(15%) nanocubes that there were indeed manganese (Mn) elements doped into the nanocubes (see the Supporting Information, Figure S3). Inductively coupled plasma (ICP-AES) was employed (see the Supporting Information, Table S1) to quantify the final doping ratios of Mn^{2+} in PB:Mn nanocubes. With the increasing amount of added $MnCl_2$, more Mn^{2+} was doped into the nanocubes, with the eventual Mn^{2+} doping ratios $([Mn]/([Fe] + [Mn]))$ measured to be 4.1, 15.3, and 26.8% for PB:Mn(5%), PB:Mn(15%), and PB:Mn(25%) respectively. Fourier transform Infrared (FT-IR) spectra were recorded for PB and PB:Mn samples (see the Supporting Information, Figure S4). According to literature, typical vibration bands of Fe^{3+}-NC-Fe^{2+} and Mn^{2+}-NC-Fe^{2+}, which locate at 2074 and 2067 cm^{-1}, respectively,[33,34] could hardly be separated in the IR spectrum and would appear as a superimposed and broad band with two contributions of asymmetric vibrations of the bridged cyanides Mn^{2+}-NC-Fe^{2+} and Fe^{3+}-NC-Fe^{2+}. As the increase of Mn^{2+} doping level, this IR band shifted to lower wavenumbers, further indicating that Fe^{3+} was partly replaced by Mn^{2+} (both with 5 unpaired 3d electrons) in the coordination structure matrix of PB:Mn samples.[36,37]

The optical properties of the obtained PB:Mn nanocubes were then studied. Figure 1f showed the UV−vis−NIR spectra of PB:Mn nanocubes with the same total metal ion concentrations (a sum of $[Fe] + [Mn]$). A broad absorption band from 500 to 900 nm with a strong absorption peak at 704 nm was observed for PB nanocubes, corresponding to the energy of the metal-to-metal charge transfer (MMCT) between Fe^{2+} and Fe^{3+} through the cyanide bridge.[33] Interestingly, after doping Mn^{2+} into PB nanocubes, it was found that the color of the solution also changed from blue to green with the increasing of Mn^{2+} doping ratio, and the absorbance peak was obviously red-shifted to 718, 730, and 768 nm for
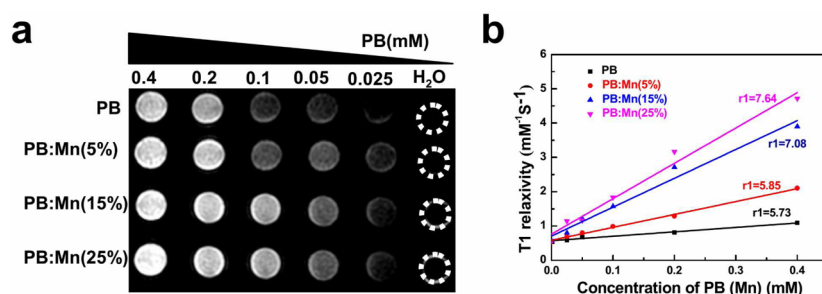
Figure 2. Enhanced MR contrast ability of PB:Mn nanocubes. (a) T1-weighted MR images of PB:Mn nanocubes with various concentrations. (b) PB:Mn nanocubes concentration dependent T1 relaxation rates. The longitudinal relaxivities (r1) were determined to be 5.73, 5.85, 7.08, and 7.64 mM^{-1} S^{-1}, for PB, PB:Mn(5%), PB:Mn(15%), and PB:Mn(25%), respectively.
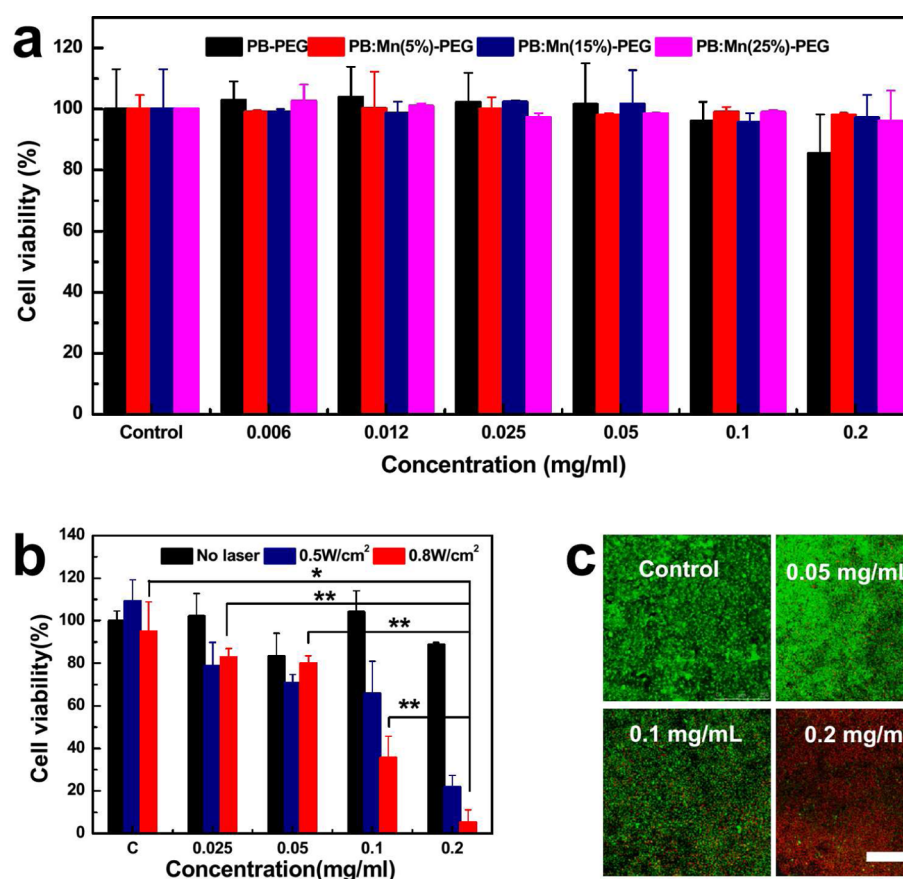

Figure 3. In vitro cell experiments. (a) Relative viabilities of 4T1 cells after incubation with PEGylated PB and PB:Mn nanocubes for 24 h with different concentrations. (b) Relative viabilities of 4T1 cells after photothermal ablation induced by PB:Mn(15%)-PEG with 808 nm laser irradiation at the power densities of 0.5 and 0.8 W/cm^2 for 5 min. Error bars were collected based on the standard deviations (STDEV) of six parallel samples. P values were calculated by the methodology of Tukey's post-test (***$p < 0.001$, **$p < 0.01$, or *$p < 0.05$). (c) Confocal fluorescence images of Calcein AM/PI costained 4T1 cells post photothermal treatment induced by PB:Mn(15%)-PEG under laser irradiation at 0.8W/cm^2 for 5 min. Live and dead cells were stained by Calcein AM and PI, and presented in green and red colors in those images, respectively. Enhanced cancer cell killing was observed as the increase of PB:Mn(15%)-PEG concentrations. The scale bar is 250 μm.

PB:Mn(5%), PB:Mn(15%), and PB:Mn(25%), respectively. This red-shifted absorbance in PB:Mn samples could be explained by changes in the electron density and orbital energies of the cyanide bonds due to the presence of Mn^{2+} in the lattice.[38,39]

NIR lasers are preferred over visible lasers in PTT to achieve deeper tissue penetration. 808 nm is one of the most frequently used wavelengths for NIR lasers used in photothermal tumor ablation. Thus, we compared the optical absorption of PB:Mn samples with different Mn doping ratios at 808 nm (Figure 1g). It was found under the same concentration, the PB:Mn(15%)

sample exhibited the highest absorption at 808 nm, with a mass extinction coefficient measured to be ~25.22 cm^{-1} mg^{-1} L, which was higher than that of the other three samples at 17.5, 17.68, and 21.36 cm^{-1} mg^{-1} L for PB:Mn(5%), PB:Mn(15%), and PB:Mn(25%), respectively. As expected, PB:Mn(15%) with higher NIR absorbance offered enhanced photothermal heating performance compared to bare PB nanocubes under the 808 nm NIR laser irradiation (Figure 1h). We have also investigated the photothermal stability of PB:Mn (15%) NCs under the NIR laser irradiation compared with Indocyanine green (ICG), another FDA-approved NIR-absorbing agent also extensively
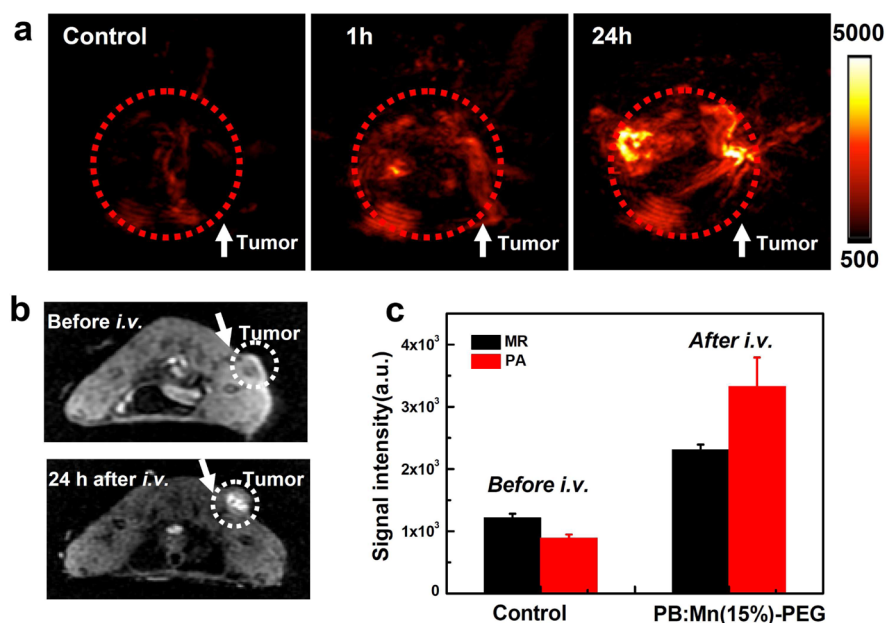
Figure 4. In vivo photoacoustic and MR imaging. (a) 2D photoacoustic imaging of tumors before and after injection of PB:Mn(15%)-PEG taken at different time points. (b) In vivo T1-weighted MR images of a mouse taken before injection (upper) and 24 h post injection (bottom) of PB:Mn(15%)-PEG. Obvious brightening effect showed up in the tumor after i.v. injection of PB:Mn(15%)-PEG. (c) T1-weighted MR signal intensities and PA signal intensities in the tumor before injection and 24 h post injection of PB:Mn(15%)-PEG.

been used as a photothermal agent. It was found the PB: Mn (15%) NCs appeared to be highly photostable under constant NIR laser exposure compared with ICG, which was easily photobleached (see the Supporting Information, Figure S5).

In the structure of pure PB nanocubes, Fe^{2+} is carbon-bonded with low spin ($S = 0$) while Fe^{3+} is nitrogen bonded with a high spin ($S = 5/2$). Thus, the nanocubes would have the ability to shorten the longitudinal relaxation times (T1) of protons in bulk water. Meanwhile, Mn^{2+} has also been demonstrated to have the ability to shorten the longitudinal relaxation T1 times of photons from bulk water.[24,35] Thus, the doping of Mn^{2+} into PB nanocubes may enhance their T1 contrasting ability during MR imaging. To study the MR contrast effects of Mn^{2+}-doped PB nanocubes, we diluted PB, PB:Mn(5%), PB:Mn(15%), and PB:Mn(25%) samples into five concentrations for MR scanning using a scanner with a magnetic field of 3 T. Obvious concentration dependent brightening effects were also observed in vitro T1-weighted MR images of those samples (Figure 2a). The obtained relaxation time T1 values were recorded and plotted as 1/T1 versus the molar concentration of total metal ions (Figure 2b). The concentration-normalized r1 relativity values were measured to be 5.73, 5.85, 7.08, and 7.64 mM^{-1} S^{-1}, for PB, PB:Mn(5%), PB:Mn(15%), and PB:Mn(25%), respectively. Thus, Mn^{2+} doping was able to obviously enhance the longitudinal relaxivity r1 of PB nanocubes for better contrast in T1-weighted MR imaging.[40,41]

Considering the fact that PB:Mn(15%) nanocubes have the highest absorption at 808 nm and a relatively high r1 value among different formulations of PB:Mn nanotubes with varied ratios of Mn-doping, we thus chose PB:Mn(15%) for further experiments. Although as-made PB:Mn nanocubes could be well-dispersed in water, they would aggregate in the presence of salts under physiological environments (see the Supporting Information, Figure S6). Therefore, ahead of applying PB:Mn(15%) nanocubes for in vitro and in vivo experiments,

we carried out surface modification through a layer-by-layer (LBL) polymer coating method (Figure 1a). On the basis of the attraction force between positive and negative charges, a cationic polymer PAH was used to coat bare PB:Mn(15%) nanocubes, switching the surface charges of nanoparticles from negative to positive (zeta potential from −23.5 mV to 17.9 mV). Then an anionic polymer PAA was utilized to coat the PB:Mn(15%)-PAH also by eletrostastatic attraction. Amino group-terminated PEG ($M_w \approx 5000$) was then conjugated to the carboxyl groups on the PB:Mn(15%)-PAH-PAA surface via amide formation. As expected, LBL coating of polymers with counter charges could lead to the switch of zeta potentials and increase of hydrodynamic diameters of those nanoparticles after each layer of polymer coating (see Supporting Information, Figures S7 and S8), confirming the successful surface decoration. The final product, PEGylated PB:Mn nanocubes (PB:Mn-PEG), exhibited a zeta potential at −10.2 mV and a hydrodynamic size of ∼122 nm and appeared to be highly stable in various physiological solutions (see the Supporting Information, Figures S6 and S9, inset).

Next, we evaluated the potential toxicity of PEGylated PB:Mn nanocubes to cells by the standard cell viability MTT assay. Various concentrations of PB−PEG, PB:Mn(5%)-PEG, PB:Mn(15%)-PEG, and PB:Mn(25%)-PEG were incubated with 4T1 cells (murine breast cancer cells) for 24 h. It was found that PEGylated PB:Mn nanocubes regardless of Mn-doping ratios all showed low toxicity to cells even at a high concentration of 0.2 mg/mL (Figure 3a). Next, we tested the internalization of PB:Mn (15%)-PEG within 4T1 cells by measuring the content of Fe element with ICP-AES. The results indicated that internalization did occur after incubating cells with PB:Mn (15%)-PEG NCs (see the Supporting Information, Figure S10). The MTT assay was then implemented to study the PTT efficacy in vitro. 4T1 cells were incubated with different concentrations of PB:Mn(15%)-PEG nanocubes for 4 h and then irradiated by an 808 nm laser
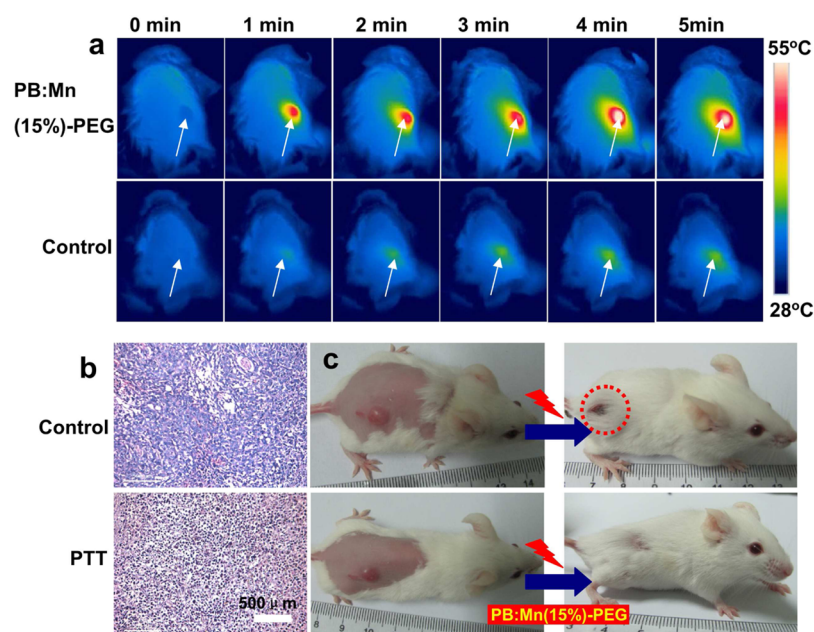
Figure 5. In vivo PTT by using PB:Mn(15%)-PEG. (a) IR thermal images of 4T1 tumor-bearing mice recorded by an IR camera. The dose of PB:Mn(15%)-PEG was 20 mg kg^{-1} in this experiment. Laser irradiation was conducted by using 808 nm NIR laser at the power density of 0.8 W/cm^2 for 5 min on the tumors. (b) H&E-stained tumor slices collected 24 h after laser irradiation from mice in control group (upper one) and PTT group (below one). The scale bar: 500 μm. (c) Photos of mice in the control group and experiment group before and 18 days after PTT.

at power densities of 0.5 and 0.8 W/cm^2. Cells were then incubated for another 24 h before measuring the viabilities by a standard MTT assay. Apparently, much more cells were killed with the increase of laser power densities and concentrations of PB:Mn(15%)-PEG nanocubes. Statistical analysis in the data of MTT was based on the methodology of Tukey's post-test (***$p < 0.001$, **$p < 0.01$, or *$p < 0.05$) (Figure 3b). Calcein-AM/PI dual staining was carried out as well to differentiate the live and dead cells. As the increase of nanocube concentration, more cells were killed after laser irradiation (Figure 3c). All these results confirmed that PB:Mn(15%)-PEG nanocubes had a great potential for photothermal ablation of cancer cells under the NIR laser irradiation.

Before moving forward to study the in vivo photothermal efficacy by using PB:Mn(15%)-PEG nanocubes, in vivo bimodal imaging on mice intravenously (i.v.) injected with PB:Mn(15%)-PEG was first carried out. First, PA imaging, which is a recently emerged imaging modality with improved in vivo spatial resolution and tissue penetration compared to traditional optical imaging techniques,[42−44] was carried out at different time points after i.v. injection. The intrinsic signals from blood vasculature were observed at the tumor site before i.v. injection of PB:Mn(15%)-PEG. After injection, the tumor signals were greatly enhanced (Figure 4a). Strong PA signals appeared throughout the whole tumor at 24 h post injection (p.i.), suggesting efficient accumulation of PB:Mn(15%)-PEG inside the tumor as a result of enhanced permeability and retention (EPR) effect of cancerous tumors.[45,46]

Next, in vivo MR imaging was conducted utilizing the strong T1 contrast offered by PB:Mn(15%)-PEG. A noticeable brightening effect at the tumor site was observed after i.v. injection of PB:Mn(15%)-PEG into 4T1 tumor-bearing mice at 24 h p.i.(Figure 4b). On the basis of region-of-interest (ROI) quantification, the quantitative MR/PA imaging results further verified that both signals were obviously increased in the tumor region after i.v. injection of PB:Mn(15%)-PEG (Figure 4c).

Therefore, both in vivo PA and MR images verified the efficient tumor passive targeting of PB:Mn(15%)-PEG after i.v. injection.

Inspired by the fascinating in vitro photothermal effect and the efficient tumor accumulation of PB:Mn(15%)-PEG, we then conducted the animal experiments to realize in vivo PTT by using PB:Mn(15%)-PEG.[47,48] Eight 4T1 tumor-bearing mice were divided into two groups, with one group i.v. injected with PB:Mn(15%)-PEG nanocubes and the other group used as the control. Twenty-four hours after injection, an 808 nm laser with a power density of 0.8 W/cm^2 was applied to irradiate the tumors for 5 min. At the same time, an IR thermal camera was used to monitor the tumor temperature during the photothermal process. It was found that the surface temperature of the tumor on mice treated with PB:Mn(15%)-PEG rapidly increased from 28 °C to ∼55 °C during laser irradiation. In contrast, the mice without injection of PB:Mn(15%)-PEG showed no apparent heating effect (Figure 5a).

To assess the photothermal ablation effort toward tumors, we sacrificed two mice from each group after 24 h with tumor sliced and stained by H&E. Because of he hyperthermia produced by PB:Mn(15%)-PEG under laser irradiation, an obvious damage to tumor cells was noticed on the mouse with injection of PB:Mn(15%)-PEG, quite different from the other control group which retained the normal morphology of tumor cells (Figure 5b). All tumors in the PB:Mn(15%)-PEG treated group were effectively inhibited post laser irradiation (Figure 5c). The mice left in the two groups were also sacrificed after 18 days. Major organs of mice were sliced and stained by H&E for histology analysis. No noticeable organ damage or inflammatory lesion was observed in all major organs of mice receiving PB:Mn(15%)-PEG injection and photothermal treatment (see Supporting Information, Figure S11), preliminarily verified that PB:Mn(15%)-PEG nanocubes rendered no obvious toxic side effect to the mice in the short term at our tested dose.

CONCLUSION

In this work, a multifunctional nanoplatform based on Mn^{2+} doped PB (PB:Mn) nanocubes for bimodal imaging and PTT with enhanced performance was demonstrated. In this system, doping Mn^{2+} into PB nanocubes led to a higher absorption at NIR and a stronger T1-MR contrast ability. Surface modification was successfully carried out on PB:Mn nanocubes, improving their stability in physiological conditions. Biomodal PA/MR imaging was conducted, revealing the effective tumor accumulation of those nanocubes after i.v. injection. Effective in vivo PTT was further demonstrated with i.v. injection of PB:Mn(15%)-PEG and NIR laser irradiation of tumors. No obvious toxicity was observed on those mice after injection of PB:Mn (15%)-PEG nanocubes. Our results successfully demonstrated that doping Mn^{2+} into PB nanocubes can achieve both enhanced T1-MR contrasting effect and improved NIR absorption, which are favorable for future imaging-guided photothermal cancer therapy.

ASSOCIATED CONTENT

ⓢ Supporting Information

Molar extinction coefficients of PB:Mn nanocubes, size distributions of PB:Mn nanocubes, EDX spectra and XRD spectra, Fourier transform infrared spectra, DLS of PB:Mn nanocubes, zeta potentials and UV−vis absorption spectra and photos of PB:Mn(15%)-PEG in different solutions including water, PBS, FBS, and 1640 cell medium. The Supporting Information is available free of charge on the ACS Publications website at DOI: 10.1021/acsami.5b02510.

AUTHOR INFORMATION

Corresponding Author
*E-mail: lcheng2@suda.edu.cn.
Author Contributions
[†]W.Z. and K.L. contributed equally to this work.
Notes
The authors declare no competing financial interest.

ACKNOWLEDGMENTS

REFERENCES

(1) Buser, H. J.; Schwarzenbach, D.; Petter, W.; Ludi, A. The Crystal Structure of Prussian Blue: Fe4[Fe(CN)6]3.xH2O. *Inorg. Chem.* **1977**, *16*, 2704−2710.

(2) Fiorito, P. A.; Gonçales, V. R.; Ponzio, E. A.; de Torresi, S. I. C. Synthesis, Characterization and Immobilization of Prussian Blue Nanoparticles. A Potential Tool for Biosensing Devices. *Chem. Commun.* **2005**, *3*, 366−368.

(3) Fu, G.; Liu, W.; Feng, S.; Yue, X. Prussian Blue Nanoparticles Operate as A New Generation of Photothermal Ablation Agents for Cancer Therapy. *Chem. Commun.* **2012**, *48*, 11567−11569.

(4) Cheng, L.; Gong, H.; Zhu, W.; Liu, J.; Wang, X.; Liu, G.; Liu, Z. PEGylated Prussian Blue Nanocubes as A Theranostic Agent for Simultaneous Cancer Imaging and Photothermal Therapy. *Biomaterials* **2014**, *35*, 9844−9852.

(5) Cheng, L.; Wang, C.; Feng, L.; Yang, K.; Liu, Z. Functional Nanomaterials for Phototherapies of Cancer. *Chem. Rev.* **2014**, *114*, 10869−10939.

(6) Robinson, J. T.; Tabakman, S. M.; Liang, Y.; Wang, H.; Sanchez Casalongue, H.; Vinh, D.; Dai, H. Ultrasmall Reduced Graphene Oxide with High Near-Infrared Absorbance for Photothermal Therapy. *J. Am. Chem. Soc.* **2011**, *133*, 6825−6831.

(7) Yang, K.; Hu, L.; Ma, X.; Ye, S.; Cheng, L.; Shi, X.; Li, C.; Li, Y.; Liu, Z. Multimodal Imaging Guided Photothermal Therapy Using Functionalized Graphene Nanosheets Anchored with Magnetic Nanoparticles. *Adv. Mater.* **2012**, *24*, 1868−1872.

(8) Yang, K.; Wan, J.; Zhang, S.; Tian, B.; Zhang, Y.; Liu, Z. The Influence of Surface Chemistry and Size of Nanoscale Graphene Oxide on Photothermal Therapy of Cancer Using Ultra-low Laser Power. *Biomaterials* **2012**, *33*, 2206−2214.

(9) Yang, K.; Feng, L.; Shi, X.; Liu, Z. Nano-Graphene in Biomedicine: Theranostic Applications. *Chem. Rev. Soc.* **2013**, *42*, 530−547.

(10) Fazal, S.; Jayasree, A.; Sasidharan, S.; Koyakutty, M.; Nair, S. V.; Menon, D. Green Synthesis of Anisotropic Gold Nanoparticles for Photothermal Therapy of Cancer. *ACS Appl. Mater. Interfaces* **2014**, *6*, 8080−8089.

(11) Huang, P.; Pandoli, O.; Wang, X.; Wang, Z.; Li, Z.; Zhang, C.; Chen, F.; Lin, J.; Cui, D.; Chen, X. Chiral Guanosine 5′-Monophosphate-Capped Gold Nanoflowers: Controllable Synthesis, Characterization, Surface-Enhanced Raman Scattering Activity, Cellular Imaging and Photothermal Therapy. *Nano Res.* **2012**, *5*, 630−639.

(12) Lin, M.; Guo, C.; Li, J.; Zhou, D.; Liu, K.; Zhang, X.; Xu, T.; Zhang, H.; Wang, L.; Yang, B. Polypyrrole-Coated Chainlike Gold Nanoparticle Architectures with the 808 nm Photothermal Transduction Efficiency up to 70%. *ACS Appl. Mater. Interfaces* **2014**, *6*, 5860−5868.

(13) Huang, X.; El-Sayed, I. H.; Qian, W.; El-Sayed, M. A. Cancer Cell Imaging and Photothermal Therapy in the Near-Infrared Region by Using Gold Nanorods. *J. Am. Chem. Soc.* **2006**, *128*, 2115−2120.

(14) Tong, L.; Wei, Q.; Wei, A.; Cheng, J. X. Gold Nanorods as Contrast Agents for Biological Imaging: Optical Properties, Surface Conjugation and Photothermal Effects. *Photochem. Photobiol.* **2009**, *85*, 21−32.

(15) Tang, S.; Huang, X.; Zheng, N. Silica Coating Improves the Efficacy of Pd Nanosheets for Photothermal Therapy of Cancer Cells Using Near Infrared Laser. *Chem. Commun.* **2011**, *47*, 3948−3950.

(16) Song, G.; Shen, J.; Jiang, F.; Hu, R.; Li, W.; An, L.; Zou, R.; Chen, Z.; Qin, Z.; Hu, J. Hydrophilic Molybdenum Oxide Nanomaterials with Controlled Morphology and Strong Plasmonic Absorption for Photothermal Ablation of Cancer Cells. *ACS Appl. Mater. Interfaces* **2014**, *6*, 3915−3922.

(17) Li, Y.; Lu, W.; Huang, Q.; Li, C.; Chen, W. Copper Sulfide Nanoparticles for Photothermal Ablation of Tumor Cells. *Nanomedicine* **2010**, *5*, 1161−1171.

(18) Cheng, L.; Liu, J.; Gu, X.; Gong, H.; Shi, X.; Liu, T.; Wang, C.; Wang, X.; Liu, G.; Xing, H. PEGylated WS2 Nanosheets as a Multifunctional Theranostic Agent for in vivo Dual-Modal CT/Photoacoustic Imaging Guided Photothermal Therapy. *Adv. Mater.* **2014**, *26*, 1886−1893.

(19) Li, B.; Ye, K.; Zhang, Y.; Qin, J.; Zou, R.; Xu, K.; Huang, X.; Xiao, Z.; Zhang, W.; Lu, X. Photothermal Theragnosis Synergistic Therapy Based on Bimetal Sulphide Nanocrystals Rather Than Nanocomposites. *Adv. Mater.* **2015**, DOI: 10.1002/adma.201404257.

(20) Xue, P.; Cheong, K. K.; Wu, Y.; Kang, Y. An In-Vitro Study of Enzyme-Responsive Prussian Blue Nanoparticles for Combined Tumor Chemotherapy and Photothermal Therapy. *Colloid and Surfaces B: Biointerfaces* **2015**, *125*, 277−283.

(21) Hoffman, H. A.; Chakrabarti, L.; Dumont, M. F.; Sandler, A. D.; Fernandes, R. Prussian Blue Nanoparticles for Laser-Induced Photothermal Therapy of Tumors. *RSC Adv.* **2014**, *4*, 29729−29734.

(22) Wu, M.; Wang, Q.; Liu, X.; Liu, J. Highly Efficient Loading of Doxorubicin in Prussian Blue Nanocages for Combined Photothermal/Chemotherapy against Hepatocellular Carcinoma. *RSC Adv.* **2015**, *5*, 30970−30980.

(23) Jia, X.; Cai, X.; Chen, Y.; Wang, S.; Xu, H.; Zhang, K.; Ma, M.; Wu, H.; Shi, J.; Chen, H. Perfluoropentane-Encapsulated Hollow Mesoporous Prussian Blue Nanocubes for Activated Ultrasound Imaging and Photothermal Therapy of Cancer. *ACS Appl. Mater. Interfaces* **2015**, *7*, 4579−4588.

(24) Shokouhimehr, M.; Soehnlen, E. S.; Hao, J.; Griswold, M.; Flask, C.; Fan, X.; Basilion, J. P.; Basu, S.; Huang, S. D. Dual Purpose Prussian Blue Nanoparticles for Cellular Imaging and Drug Delivery: A New Generation of T 1-Weighted MRI Contrast and Small Molecule Delivery Agents. *J. Mater. Chem.* **2010**, *20*, 5251−5259.

(25) Song, Z.; Yuan, R.; Chai, Y.; Yin, B.; Fu, P.; Wang, J. Multilayer Structured Amperometric Immunosensor Based on Gold Nanoparticles and Prussian Blue Nanoparticles/Nanocomposite Functionalized Interface. *Electrochim. Acta* **2010**, *55*, 1778−1784.

(26) Hu, M.; Furukawa, S.; Ohtani, R.; Sukegawa, H.; Nemoto, Y.; Reboul, J.; Kitagawa, S.; Yamauchi, Y. Synthesis of Prussian blue Nanoparticles with a Hollow Interior by Controlled Chemical Etching. *Angew. Chem., Int. Ed.* **2012**, *124*, 1008−1012.

(27) Jing, L.; Liang, X.; Deng, Z.; Feng, S.; Li, X.; Huang, M.; Li, C.; Dai, Z. Prussian Blue Coated Gold Nanoparticles for Simultaneous Photoacoustic/CT Bimodal Imaging and Photothermal Ablation of Cancer. *Biomaterials* **2014**, *35*, 5814−5821.

(28) Maurin-Pasturel, G.; Long, J.; Guari, Y.; Godiard, F.; Willinger, M.-G.; Guerin, C.; Larionova, J. Nanosized Heterostructures of Au@ Prussian Blue Analogues: Towards Multifunctionality at the Nanoscale. *Angew. Chem., Int. Ed.* **2014**, *53*, 3872−3876.

(29) Sharma, V.; Mitra, S.; Kumar, A.; Yusuf, S.; Juranyi, F.; Mukhopadhyay, R. Diffusion of Water in Molecular Magnet Cu0. 75Mn0. 75 [Fe (CN) 6]·7H2O. *J. Phys.: Condens. Matter* **2011**, *23*, 446002.

(30) Tokoro, H.; Shiro, M.; Hashimoto, K.; Ohkoshi, S. i. Single Crystal of a Prussian Blue Analog based on Rubidium Manganese Hexacyanoferrate. *Z. Anorg. Allg. Chem.* **2007**, *633*, 1134−1136.

(31) Dumont, M. F.; Yadavilli, S.; Sze, R. W.; Nazarian, J.; Fernandes, R. Manganese-Containing Prussian Blue Nanoparticles for Imaging of Pediatric Brain Tumors. *Int. J. Nanomed.* **2014**, *9*, 2581.

(32) Li, Y.; Li, C. H.; Talham, D. R. One-step Synthesis of Gradient Gadolinium Ironhexacyanoferrate Nanoparticles: A New Particle Design Easily Combining MRI Contrast and Photothermal Therapy. *Nanoscale* **2015**, *7*, 5209−5216.

(33) Dumont, M. F.; Hoffman, H. A.; Yoon, P. R. S.; Conklin, L. S.; Saha, S. R.; Paglione, J.; Sze, R. W.; Fernandes, R. Biofunctionalized Gadolinium-Containing Prussian Blue Nanoparticles as Multimodal Molecular Imaging Agents. *Bioconjugate Chem.* **2013**, *25*, 129−137.

(34) Paul, G.; Prado, Y.; Dia, N.; Rivière, E.; Laurent, S.; Roch, M.; Vander Elst, L.; Muller, R. N.; Sancey, L.; Perriat, P. Mn II-Containing Coordination Nanoparticles as Highly Efficient T 1 Contrast Agents for Magnetic Resonance Imaging. *Chem. Commun.* **2014**, *50*, 6740−6743.

(35) Shokouhimehr, M.; Soehnlen, E. S.; Khitrin, A.; Basu, S.; Huang, S. D. Biocompatible Prussian Blue Nanoparticles: Preparation, Stability, Cytotoxicity, and Potential Use as An MRI Contrast Agent. *Inorg. Chem. Commun.* **2010**, *13*, 58−61.

(36) Okubo, M.; Asakura, D.; Mizuno, Y.; Kim, J.-D.; Mizokawa, T.; Kudo, T.; Honma, I. Switching Redox-Active Sites by Valence Tautomerism in Prussian Blue Analogues A x Mn y [Fe (CN) 6]· n H2O (A: K, Rb): Robust Frameworks for Reversible Li Storage. *J. Phys. Chem. Lett.* **2010**, *1*, 2063−2071.

(37) Buschmann, W. E.; Ensling, J.; Gütlich, P.; Miller, J. S. Electron Transfer, Linkage Isomerization, Bulk Magnetic Order, and Spin-Glass Behavior in the Iron Hexacyanomanganate Prussian Blue Analogue. *Chem.—Eur. J.* **1999**, *5*, 3019−3028.

(38) Wojdel, J. C.; Bromley, S. T. Band Gap Variation in Prussian Blue via Cation-Induced Structural Distortion. *J. Phys. Chem. B* **2006**, *110*, 24294−24298.

(39) Cafun, J.-D.; Champion, G.; Arrio, M.-A.; dit Moulin, C. C.; Bleuzen, A. Photomagnetic CoFe Prussian Blue Analogues: Role of the Cyanide Ions as Active Electron Transfer Bridges Modulated by Cyanide-Alkali Metal Ion Interactions. *J. Am. Chem. Soc.* **2010**, *132*, 11552−11559.

(40) Lin, Y.-J.; Koretsky, A. P. Manganese Ion enhances T1-Weighted MRI During Brain Activation: An Approach to Direct Imaging of Brain Function. *Magn. Reson. Med.* **1997**, *38*, 378−388.

(41) Fu, G.; Liu, W.; Li, Y.; Jin, Y.; Jiang, L.; Liang, X.; Feng, S.; Dai, Z. Magnetic Prussian Blue Nanoparticles for Targeted Photothermal Therapy under Magnetic Resonance Imaging Guidance. *Bioconjugate Chem.* **2014**, *25*, 1655−1663.

(42) Cai, X.; Jia, X.; Gao, W.; Zhang, K.; Ma, M.; Wang, S.; Zheng, Y.; Shi, J.; Chen, H. A Versatile Nanotheranostic Agent for Efficient Dual-Mode Imaging Guided Synergistic Chemo-Thermal Tumor Therapy. *Adv. Funct. Mater.* **2015**, DOI: 10.1002/adfm.201403991.

(43) Wang, X.; Pang, Y.; Ku, G.; Xie, X.; Stoica, G.; Wang, L. V. Noninvasive Laser-Induced Photoacoustic Tomography for Structural and Functional In Vivo Imaging of the Brain. *Nat. Biotechnol.* **2003**, *21*, 803−806.

(44) Maji, S. K.; Sreejith, S.; Joseph, J.; Lin, M.; He, T.; Tong, Y.; Sun, H.; Yu, S. W. K.; Zhao, Y. Upconversion Nanoparticles as A Contrast Agent for Photoacoustic Imaging in Live Mice. *Adv. Mater.* **2014**, *26*, 5633−5638.

(45) Maeda, H.; Wu, J.; Sawa, T.; Matsumura, Y.; Hori, K. Tumor Vascular Permeability and the EPR Effect in Macromolecular Therapeutics: A Review. *J. Controlled Release* **2000**, *65*, 271−284.

(46) Fang, J.; Nakamura, H.; Maeda, H. The EPR Effect: Unique Features of Tumor Blood Vessels for Drug Delivery, Factors Involved, and Limitations and Augmentation of the Effect. *Adv. Drug Delivery Rev.* **2011**, *63*, 136−151.

(47) O'Neal, D. P.; Hirsch, L. R.; Halas, N. J.; Payne, J. D.; West, J. L. Photo-Thermal Tumor Ablation in Mice Using Near Infrared-Absorbing Nanoparticles. *Cancer Lett.* **2004**, *209*, 171−176.

(48) Zhang, Z.; Wang, J.; Chen, C. Near-Infrared Light-Mediated Nanoplatforms for Cancer Thermo-Chemotherapy and Optical Imaging. *Adv. Mater.* **2013**, *25*, 3869−3880.